

# Three dimensional linear stability analysis of the boundary and entropy layers on a hypersonic vehicle fore-body

*M. Ferrier, E. Orlik, D. Davidenko, and I. Fedioun*  
*Institut de Combustion, Aérothermique, Réactivité et Environnement (ICARE)*  
*CNRS Orléans, 1c avenue de la Recherche Scientifique*  
*F-45071 ORLEANS cedex2, France*

## Abstract

Laminar air flow developing under a hypersonic vehicle fore-body is numerically simulated using a Navier-Stokes code, and the linear stability analysis is applied accounting for the entropy layer and wall thermal conditions. The entropy layer induces an additional unstable mode. Under adiabatic wall conditions, instabilities are a combination of first oblique and crossflow modes. On cold wall, the first mode is damped and only the crossflow instability remains. Several options are investigated in the application of the  $e^N$  method. It is found that the choice of the integration path is of minor importance on the computed N factors.

## 1. Introduction

The scramjet-powered hypersonic vehicle of interest, designed by MBDA France and ONERA, is planned to fly from Mach 4 to Mach 8, at 20 to 30 km. A well adapted air inlet is of great importance for such vehicles. This implies to control the transition of the boundary layer (BL) developing under the fore-body: a turbulent boundary layer incoming the combustion chamber is more likely to avoid flow separation due to strong adverse pressure gradients.

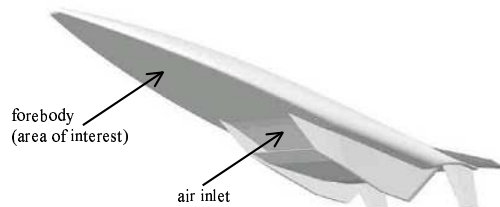


Figure 1: Artist view of the vehicle. Image ONERA-MBDA

As a first step, one must be able to predict the natural transition for flight conditions and wind-tunnel conditions. For this purpose, the Linear Stability Theory (LST) coupled to the semi-empirical ' $e^N$ ' method is still, at the moment, the only reliable tool<sup>1</sup>. A previous study<sup>2</sup> has shown that the LST can be successfully applied to laminar flow profiles obtained from Navier-Stokes calculations on real configurations, with accurate temperature-dependant thermodynamics and transport properties. Nevertheless, two specific points are still to be addressed:

(i): The blunt leading edge of the vehicle induces a bow shock and consequently an entropy layer (EL) that merges downstream with the boundary layer (BL). How does the entropy layer modify the boundary layer stability properties? More precisely, which part of the near-wall flow profiles should be retained for the stability analysis?

(ii): In the case of simple geometries like sharp cones at zero angle of attack or flat plates, the direction in which unstable waves are amplified is aligned with the mean flow. Hence, both the amplification direction  $\bar{\psi}$  (see section 3) and the integration path for the computation of N factors are clearly defined. This is no longer the case for a 3D flow. How to specify physically these parameters? Are the computed N values very dependent on these choices?

In section 2, the Navier-Stokes mean flow calculation will be described, showing the topology of the flow. In section 3, the LST will be recalled briefly, and the influence of the EL will be discussed in reference to the Lees & Lin<sup>3</sup> asymptotic analysis. Finally stability results will be presented in section 4.

## 2. Calculation of the mean flow

The laminar mean flow corresponds to flight conditions at Mach 6 and 25km. According to the 1976 standard atmosphere, static temperature and pressure are respectively 221.6 K and 2512 Pa. The stagnation temperature is about 1800K, too low to produce the dissociation of di-oxygen, but high enough to need accurate thermodynamic and transport coefficients, to which the LST calculations are very sensitive. Calculations have been done using the GAMBIT<sup>®</sup> 2.30 and FLUENT<sup>®</sup> 6.2.16 commercial codes.

### 2.1 Thermodynamic and transport model

Air is considered as a mixture of N<sub>2</sub> (78.0840%), O<sub>2</sub> (20.9476%), Argon (0.9365%) and CO<sub>2</sub> (0.0319%), as defined in Alexander Burcat's thermodynamics database (<http://garfield.chem.elte.hu/Burcat/burcat.html>). Using Burcat's data, the molar mass of air is  $M_{air} = 28.965$  kg/kmol. Isobaric heat capacities of single components are approximated by 4<sup>th</sup> order polynomials fits for two ranges of temperature: 200K-1000K and 1000K-6000K. Since the static temperature is in the low-range limit, only the high temperature range is retained from Burcat. At low temperatures, data from Lemmon *et al.*<sup>4</sup>, accurate from 80K to 2000K are used instead, for N<sub>2</sub> and O<sub>2</sub> (Lemmon *et al.* do not provide any value for CO<sub>2</sub>). The two curves are matched numerically at 1000K. Then, heat capacity of air is computed from single components properties as a mole-weighted average for each temperature range. The resulting global fit is shown on figure 2.

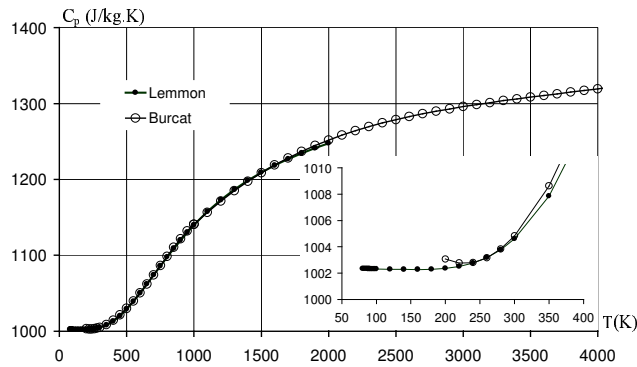


Figure 2: Heat capacity of air

The viscosity  $\mu(T)$  of air is calculated with the Wilke's mixing formula<sup>5</sup> in which single component values  $\mu_\alpha(T)$  are obtained from the CHEMKIN II<sup>6</sup> transport model based on the kinetic theory. The same method is applied for the thermal conductivity  $k(T)$  of air, changing  $\mu_\alpha(T)$  to  $k_\alpha(T)$  in the Wilke's formula. Polynomial fits accurate in the range 100K-5000K are then applied, of the 5<sup>th</sup> and 3<sup>rd</sup> orders for  $\mu$  and  $k$  respectively. Details are given in Ferrieret *al.*<sup>2</sup> The unit Reynolds number is about  $4.8 \times 10^6 \text{m}^{-1}$ .

### 2.2 Grid requirements and calculation setup

The fore-body that has been studied is about 1.3m long. The noze radius is 5mm. Upper and lower faces are plane, with an angle  $+4.8^\circ$  and  $-4^\circ$  respectively. The end section is  $0.48\text{m} \times 0.21\text{m}$ . A vertical cutting plane separates the noze region from the body region, 0.04m downstream from the noze tip (figures 3 and 4). Abscissa on the upper and lower surfaces are measured from this plane. In the noze region, the mesh is hexahedral and unstructured, and in the body region of interest for the LST calculations, the mesh is fully structured. In order to describe properly the BL, the height of the first cell is about 0.05mm all along the body, and the total number of cells is 101 from the wall to the boundary of the computational domain. The whole mesh has about  $2 \times 10^6$  cells. Calculations have been performed using the 2<sup>nd</sup> order upwind implicit density-based solver available in FLUENT<sup>®</sup> 6.2.16. The wall is considered as radiating with emmissivity  $\sigma = 0.8$ , in thermal equilibrium with the flow, which is the most representative of flight conditions. Calculations with an adiabatic wall have also been done for comparison, but on a coarser mesh in the transverse direction along the vertical plane of symmetry. Far-field non-reflecting characteristic-based boundary conditions are imposed. This boundary condition is not very accurate in the exit section, between the wall and the sonic line in the BL, but it affects only the last two rows of cells. Convergence is obtained after 15000 iterations, taking about 50h of

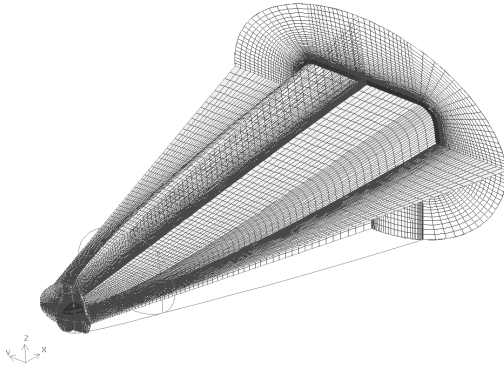


Figure 3: Overview of the  $\approx 2 \times 10^6$  cells computational mesh

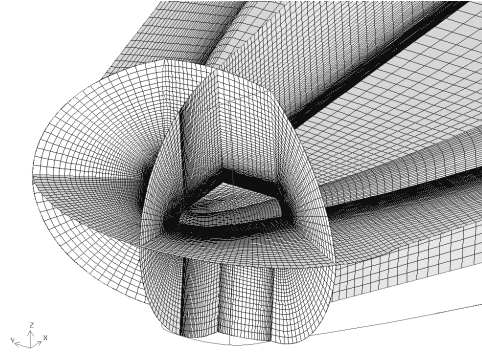


Figure 4: Detail of the unstructured mesh of the nozzle region

CPU time on 4 Intel bi-Xeon 3.2 GHz (8 processors). Convergence criteria are based on residuals, mass balance, wall temperature in the plane of symmetry of the vehicle and skin friction.

### 2.3 Topology of the flow

The fore-body is placed at an angle of attack (AOA) of  $4^\circ$ . Stream coming from the nozzle converges towards the plane of symmetry and rolls-up in a pair of counter-rotating longitudinal vortices on both sides of the symmetry plane (figures 5 and 6). Two additional smaller ones are also present, but are not visible in the figure. The fine mesh for the radiating case can capture properly these vortical structures.

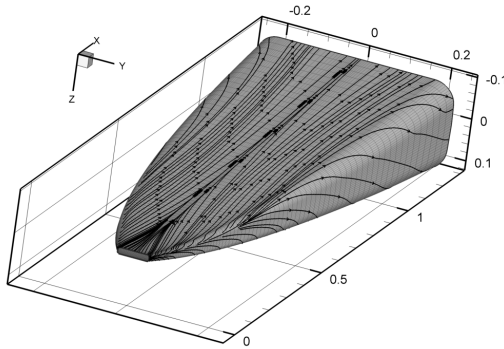


Figure 5: Streamlines under the fore-body at  $4^\circ$  AOA

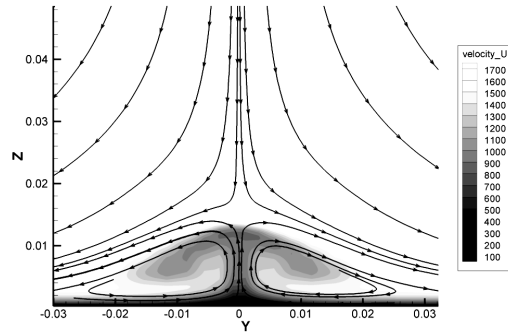


Figure 6: Longitudinal vortices on each side of the symmetry plane at  $x = 1\text{m}$

## 3. Linear Stability Theory

### 3.1 Principles

The calculated laminar mean flow is now used as input data for the stability computation, in the local LST approach. In this approach, the boundary layer is considered as a parallel flow. The stability computation can thus be processed for any location on the fore-body independently of the others. In the frame of local LST, a perturbation  $q'$  has the following shape:

$$q'(x, y, z, t) = \hat{q}(y) \exp[i(\alpha x + \beta z - \omega t)] \quad (1)$$

Let us notice that the coordinate system is different from the one used for the Navier-Stokes computations. Here,  $x$  remains the longitudinal direction of the flow,  $y$  is normal to the wall and  $z$  is the spanwise direction. The parameters  $\alpha$ ,

$\beta$  and  $\omega$  can either be real or complex, according to the nature of instabilities. Here, they are convective, so the spatial approach is adopted:  $\alpha = \alpha_r + i\alpha_i$  and  $\beta = \beta_r + i\beta_i$  are complex, and  $\omega = 2\pi f$  is real. In that case, the perturbation becomes:

$$q'(x, y, z, t) = \hat{q}(y) \exp(-\alpha_i x - \beta_i z) \exp[i(\alpha_r x + \beta_r z - \omega t)] \quad (2)$$

Then, a wave perturbation of the frequency  $f$ (Hz), propagating in the direction

$$\psi = \arctan\left(\frac{\beta_r}{\alpha_r}\right) \quad (3)$$

with the phase velocity

$$c = \frac{\omega}{\sqrt{\alpha_r^2 + \beta_r^2}} \quad (4)$$

will see its amplitude

$$A(x, z) = |\hat{q}(y)| \exp(-\alpha_i x - \beta_i z) \quad (5)$$

growing (or decreasing) with the rate

$$\begin{cases} \frac{1}{A} \frac{\partial A}{\partial x} = -\alpha_i & \text{in the } x \text{ direction} \\ \frac{1}{A} \frac{\partial A}{\partial z} = -\beta_i & \text{in the } z \text{ direction} \end{cases} \quad (6)$$

In the same way as the wave propagation angle  $\psi$ , the wave amplification angle  $\bar{\psi}$  is defined by

$$\bar{\psi} = \arctan\left(\frac{\beta_i}{\alpha_i}\right) \quad (7)$$

At each location  $(x, z)$ , the 3D linearized Navier-Stokes equations governing the small perturbations are solved using a fourth order Runge-Kutta scheme coupled with a shooting method in order to make the  $y$ -velocity perturbation  $\hat{v}(y)$  vanish at the wall, that is, to satisfy the boundary conditions. The input data for the stability code are: the near-wall flow profiles, the wave propagation and amplification angles and the wave frequency. Because of the complicated shape of certain profiles (due to the combination of BL and EL), it is difficult to determine the wall layer thickness (see figure 7). In other words, it is not clear which part of the flow should be retained to perform the stability analysis. Another difficulty is to manage the three parameters  $f$ ,  $\psi$  and  $\bar{\psi}$  in order to predict the transition. We will explain briefly in subsection 3.3 how the  $e^N$  criterion coupled with the envelop method can fix the problem for  $f$  and  $\psi$ . However, the angle of amplification  $\bar{\psi}$ , i.e. the value of  $\beta_i$  given  $\alpha_i$ , is undetermined in the theory, and no clear solution has yet been proposed in the literature. This will also be addressed in subsection 3.3.

### 3.2 Item (i) : Effect of the entropy layer

Figure 7 presents a typical velocity profile close to the plane of symmetry ( $z = 0.038m$ ), for the adiabatic wall case. Because of the entropy layer, two inflexion points arise in the profile. These inflexion points will induce extrema in the profile of the quantity  $\rho \partial U / \partial y$ , which are named "Generalized Inflexion Points" (GIP) by Lees & Lin.<sup>3</sup> According to them, the occurrence of a GIP is a sufficient condition for the existence of an unstable wave if the mean flow velocity  $U$  at the altitude  $y_s$  of the GIP is such that:

$$\frac{U(y_s)}{U^e} > 1 - \frac{1}{M^e} \quad (8)$$

where  $U^e$  and  $M^e$  are respectively the velocity and Mach number at the edge of the BL. In figure 8, the quantity  $\rho \partial U / \partial y$  is plotted for the entire profile of figure 7. One can see three GIPs, two of them verifying condition (8). The associated unstable modes will be taken into account in the stability calculation only if the profile is cut at the altitude  $Y_{c2}$ , including both BL and EL. Notice also that the choice of the altitude retained influences directly  $U^e$  and  $M^e$ .

Figures 9 and 10 show the value of the  $y$ -component of the velocity perturbation  $\hat{v}(y)$  at the wall, for different values of the couple  $(\alpha_r, \alpha_i)$  and from the velocity profile of figure 7. The dots on these maps represent numerical solutions of the dispersion relation of the flow. In other words, these two figures represent the spectrum of the linearized Navier-Stokes operator when the profile is truncated at two different altitudes from the wall ( $Y_{c1}, Y_{c2}$ ). It is clear that the part of the velocity profile that is retained has a strong influence on the stability calculations. Indeed, the number of modes is increased when the EL is taken into account. In particular, an unstable mode appears (mode 3) while modes 1 and 2 are stable for this propagation angle ( $\psi = 0$ ). The effect of this mode on the BL stability is not clear and needs further investigations. However, early computations indicate very weak  $N$  factors so we think that mode 3 is unable to provoke transition by itself. Nevertheless, it is known that a blunt nose can promote transition<sup>7,8</sup>, probably because of the EL formation. The ways the EL instabilities can affect the BL stability are still not understood and may be investigated using Direct Numerical Simulation.

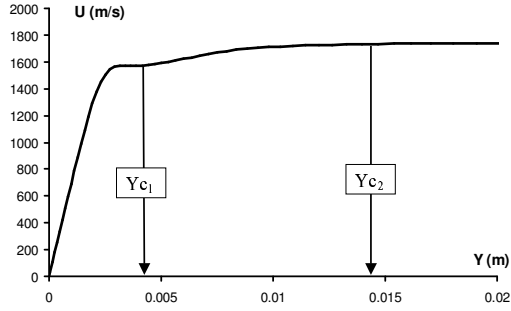


Figure 7: Velocity profiles at  $x = 0.5\text{m}$ ,  $z = 0.038\text{m}$

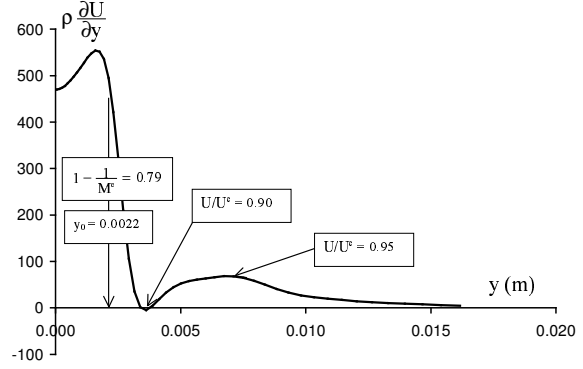


Figure 8: Generalized inflexion points

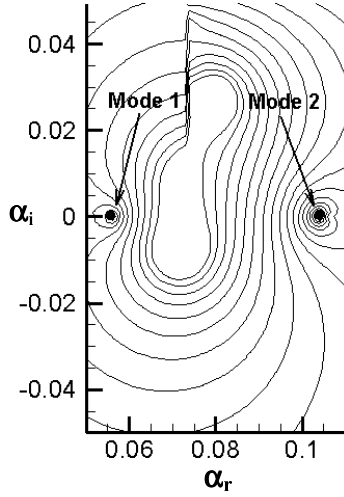


Figure 9: Spectrum of the linearized Navier-Stokes operator for the  $Y_{c1}$  cut

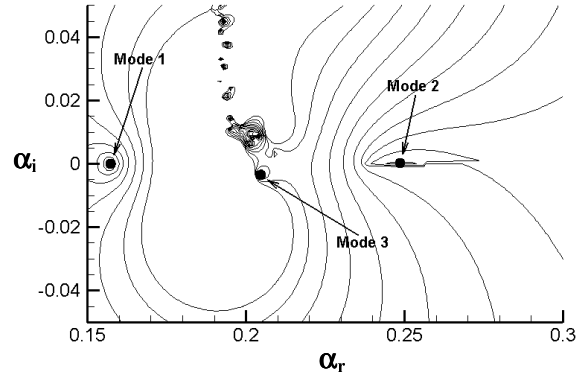


Figure 10: Spectrum of the linearized Navier-Stokes operator for the  $Y_{c2}$  cut

### 3.3 Item (ii) : $e^N$ method, envelop method, integration path

In the  $e^N$  method, amplification rates of every unstable frequencies are integrated along a path on the surface of interest (here the fore-body of the vehicle). The transition location is then determined using the upper bound curve of all unstables frequencies. In compressible or 3D flows, the most unstable wave is no longer aligned with the flow velocity outside of the boundary layer, and at each location, one possibility is to seek the angle  $\psi$  for which the wave is the most amplified (envelop method). Therefore, considering equation (6),  $N$  factors are given by:

$$N(s) = \max_{f, \psi} \int_{s_0}^s \sqrt{\alpha_i^2 + \beta_i^2} d\xi \quad (9)$$

where  $s_0$  is the point on the path, where the wave becomes unstable.

A problem remains in the coherent choice of the integration path, given the angle  $\bar{\psi}$  of amplification. As it is said in the introduction, the choice is evident in 2D problems:  $\bar{\psi} = 0$ , *integration path = mean flow direction*. This no longer the case for 3D flows, where several approaches have been proposed<sup>1</sup>. First of all, we will logically consider that the integration path is tangent to the local  $\bar{\psi}$  angle: integration follows the direction of amplification. Now, there are classically three options for  $\bar{\psi}$ :

- $\bar{\psi} = 0$ ; this approach has been proposed by Mack<sup>9</sup> for swept wings.

- $\bar{\psi} = \theta_g$ , where  $\theta_g$  is the local direction of the group velocity. This option is physically justified by the fact that, in a conservative media, the energy of a wave packet travels with its group velocity.
- $\bar{\psi} = \theta^e$ , where  $\theta^e$  is the local direction of the flow outside of the boundary layer. This avoids the calculation of the group velocity and may be justified by the observation<sup>1</sup> that  $\theta^e \approx \theta_g$ .

Most of the time, the group velocity is evaluated in the temporal approach because, in that case, the calculation is straightforward since  $\alpha$  and  $\beta$  are real. Then, the spatial stability calculation is performed (possibly with the envelop method) to get  $\alpha_i$  with  $\beta_i = \alpha_i \tan \theta_g$ . That means two successive stability calculations. However, we noticed that stability results do not depend very much on  $\bar{\psi}$  (but the determination of the velocity group is anyway important to obtain the angle  $\theta_g$  for the integration path). This is especially true for  $\bar{\psi} < 20^\circ$ , which was the case for all the calculations. Therefore, we perform the group velocity calculation using the spatial approach. By this way, we avoid the additional temporal calculation.

#### 4. Results

In the following, mode 3 found in section 3.2 is too weak and is not taken into account for the determination of  $N$  factors. Mode 1 has a phase velocity greater than  $U^e$ , which is not physically acceptable. Therefore, only mode 2 is considered hereafter. For symmetry reasons, results are calculated and presented on one half of the body.

*Effect of the wall thermal condition on stability properties* : Mappings of maximum amplification rates  $\alpha_i$  and corresponding  $\psi = \psi_M$  angles (envelop method) are displayed in figure 11 for a single frequency  $f = 10\text{kHz}$ , both for the adiabatic and radiative wall. Calculations were done with  $\bar{\psi} = 0$ . For the adiabatic case (figures on the left), calculations were not performed on the whole surface because, as it was said in subsection 2.2, mesh is coarser than in the radiative case and so, not able to capture all the features of the flow. In the radiative case (figures on the right), the white areas correspond to stable zones. The black lines are tangent to the velocity vector calculated at the cell centers of the first row above the wall. By comparison with the streamlines outside of the boundary layer (see figure 13), the flow is strongly three-dimensional close to the nose and becomes globally two-dimensional at the end of the fore-body.

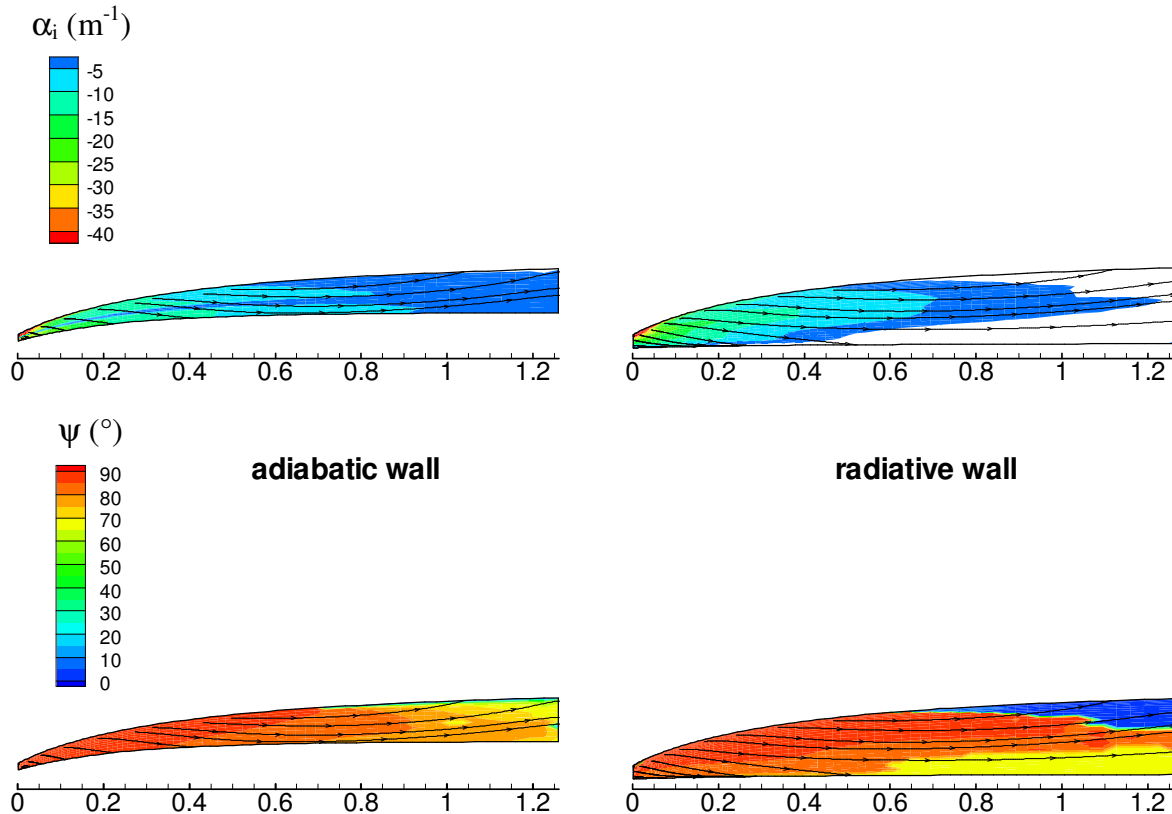


Figure 11: Comparison of  $\alpha_i$  and  $\psi_M$  between the adiabatic and radiative wall cases

In the adiabatic wall case, both the amplification rates  $\alpha_i$  and orientation of the most unstable waves  $\psi$ , decrease as the flow goes downstream. In particular,  $\psi$  values are very high close to the nose ( $85^\circ$ ) and weaker at the end of the fore-body ( $70^\circ$ ). According to these values, the instabilities are first of crossflow type (CF), and then switch to oblique first modes in Mack's classification. Results of the radiative case confirm this observation: wall cooling stabilizes the oblique first mode ( $\psi = 70^\circ$ ), in agreement with classical LST results<sup>11</sup>, but has a little effect on the CF waves ( $\psi = 80^\circ$ ). A bifurcation of the  $\psi$  behavior is also clearly visible, especially at the external border of the fore-body where the most unstable waves are first oriented at  $85^\circ$  then drop suddenly below  $5^\circ$  (blue area in the figure at the bottom on the right). This clearly shows the shift from the CF mode to the oblique first mode (that is stable in this case) towards the end of the fore-body. Finally, in some cases, we observed amplified stationary waves ( $f = 0\text{Hz}$ ) which is characteristic of CF instabilities (not presented in this paper).

*Effect of the integration strategy on computed  $N$  factors* : The three previous approaches for  $\bar{\psi}$  listed in section 3.3 are now evaluated in the case of a radiative wall, which is the most relevant for flight conditions. The following figures show the  $N$  factors for three different cases (radiative wall), according to the value of  $\bar{\psi}$  and  $\theta$ , the local tangent to the integration path: figure 12 :  $\bar{\psi} = 0$  and  $\theta = 0$ , figure 13:  $\bar{\psi} = \theta_g$  and  $\theta = \theta^e$ , figure 14:  $\bar{\psi} = \theta_g$  and  $\theta = \theta_g$ . In each figure, the black lines represent the integration path. In the second case (figure 13), the integration path is not tangent to the amplification direction ( $\bar{\psi} \neq \theta$ ), which is in contradiction with what was said in section 3. However, as already mentioned, the amplification rate depends very slightly on  $\bar{\psi}$ . In addition, the angles  $\theta_g$  and  $\theta^e$  are not much different. Therefore, in order to save one stability calculation, it was considered that stability results for  $\bar{\psi} = \theta^e$  would have been very similar to those for  $\bar{\psi} = \theta_g$ .

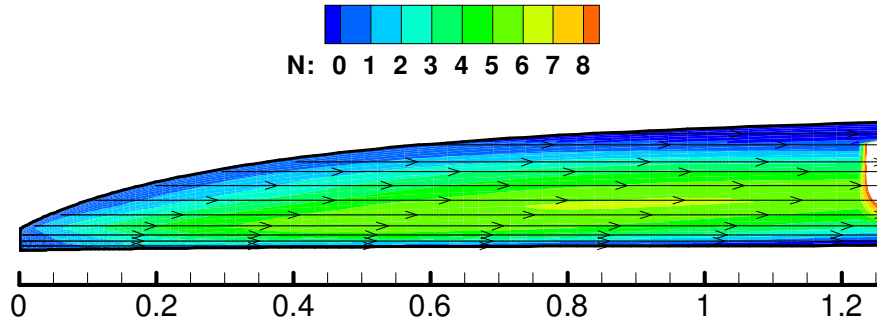


Figure 12: Integration path and  $N$  factors mapping for  $\bar{\psi} = 0$  and  $\theta = 0$

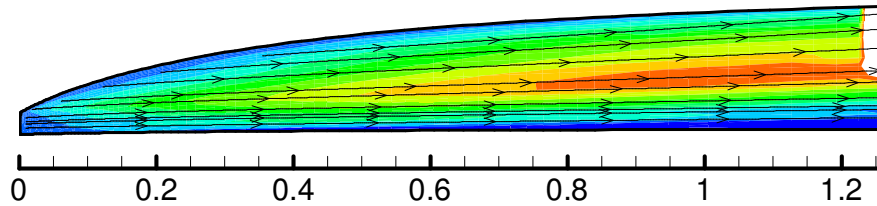


Figure 13: Same as fig.12:  $\bar{\psi} = \theta_g$  and  $\theta = \theta^e$

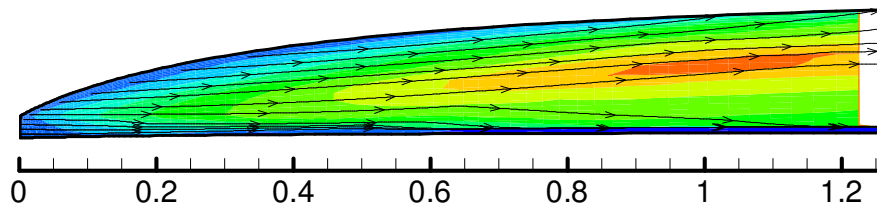


Figure 14: Same as fig.12:  $\bar{\psi} = \theta_g$  and  $\theta = \theta_g$

The maximum  $N$  factor value is about 8 in each case. This is a quite high value for CF instabilities but unfortunately hardly sufficient to trigger the transition ( $N = 10$  is the commonly accepted value in flight). Nevertheless, the

flow coming from the sides of the fore-body is not taken into account and may have an influence on the stability of the boundary layer. In figure 12 ( $\bar{\psi} = 0$ ), the maximum amplification zone spreads less than in figures 13 and 14. Regarding these two latter cases, results are almost identical. In particular, the streamlines pattern outside of the boundary layer is very similar to the pattern of the lines tangent to the group velocity (in the amplified areas), which explains the similarity between the two approaches.

## 5. Conclusion & Perspectives

The Linear Stability Theory has been applied to the near-wall flow on a full-scale hypersonic vehicle, obtained from laminar Navier-Stokes calculations. It has been shown that wall thermal conditions can change the nature of instabilities, from a combination of cross-flow and oblique first modes in case of a (hot) adiabatic wall to dominant cross-flow instability in case of a (colder) radiating wall. In the later case, several strategies of application of the  $e^N$  criterion coupled with the envelop method have shown only minor differences in the computed  $N$  factors. The total amplification observed is hardly high enough for a possible natural transition in flight. However, not all of the unstable frequencies have been taken into account, and non-linear combination of them may probably increase the  $N$  factors. This will be addressed in future work. From the theoretical point of view, it has been shown how the entropy layer introduces new generalized inflexion points in the wall flow profiles and thus additional modes of possible instability. The way these modes combine with those of the boundary layer is still unknown and out of reach of the Linear Stability Analysis. Further research will focus on this subtle issue by means of Direct Numerical Simulation.

We thank MBDA France for financial support. We thank also Eric Wendling (MBDA France), Daniel Arnal and Jean Perraud (ONERA) for helpful discussions.

## References

- [1] Arnal, D., Transition Prediction in Industrial Applications, in ‘*Transition, Turbulence and Combustion Modelling*’, *ERCOFTAC series*, Hanifi A., Alfredsson P.H., Johansson A.V. and Henningson D.S. ed., Kluwer Academic Publishers, 1998.
- [2] Ferrier, M., Fedioun, I. and Davidenko, D., Boundary Layer Prediction on a Hypersonic Vehicle Fore-body, *AIAA-2006-8092, 14th AIAA/AHI Space Planes and Hypersonic Systems and Technologies Conference*, 6-9 november 2006, Canberra, Australia
- [3] Lees, L., and Lin, C. C., Investigation of the stability of the laminar boundary layer in a compressible fluid, *NACA technical note* No. 1115, September 1946.
- [4] Lemmon, E. W. *et al.*, Thermodynamic Properties of Air and Mixtures of Nitrogen, Argon, and Oxygen From 60 to 2000K at Pressures to 2000 MPa, *J. Phys. Chem. Ref. Data*, 29(3):331-385, 2000.
- [5] Wilke, C.R., A viscosity equation for gas mixtures. *The Journal of Chemical Physics* 18(4):517-519, 1950.
- [6] Kee, R.J. *et al.*, CHEMKIN collection, release 3.5, Sandia National Laboratories, San Diego, CA, 1999.
- [7] Lysenko, V. I., Influence of the entropy layer on the stability of a supersonic shock layer and transition of the laminar boundary layer to turbulence, *Translated from Zh. Prikl. Mekh. Tekh. Fiz.*, 6:74-80, Nov-Dec 1990.
- [8] Fedorov, A., and Tumin, A., Evolution of Disturbances in Entropy Layer on Blunted Plate in Supersonic Flow, *AIAA Journal*, 42(1):89-94, 2004.
- [9] Mack, L.M., Stability of three-dimensional boundary layers on swept wings at transonic speeds, *IUTAM Symp. Transsonicum III, Göttingen*, Eds. Zierep and Oertel, Springer Verlag, 1988.
- [10] Arnal, D., Transition based on linear theory, *Progress in transition modeling*, AGARD Report No 793, 1993.
- [11] Vignau, F., Etude théorique et expérimentale de la transition en écoulement bidimensionnel compressible, *ENSAE Thesis*, 1989.



**This page has been purposely left blank**